Development of a low-profile planar sensor for the detection of normal and shear forces

Constantinos Heracleous[1,3], Julian JH Leong[2,3], Rui CV Loureiro[1,2,3]
[1] Wellcome/EPSRC Centre for Interventional and Surgical Science, University College London, London, WC1E 6BT, UK
[2] Royal National Orthopaedic Hospital, Brockley Hill, Stanmore HA7 4LP, UK
[3] Aspire Centre for Rehabilitation Engineering and Assistive Technology, University College London, HA7 4LP, UK
Constantinos.Heracleous.18@ucl.ac.uk

***Abstract*— Individuals with balance and mobility problems might benefit by the use of devices that detect small changes in ground reaction forces and potentially be used to assist movement. For maximum effectiveness, such sensors must measure pressure in all three dimensions. Impact and shear plantar force are essential variables in inverse dynamics reconstructions of the human joint force. Various force sensors have been proposed to monitor plantar forces of the human foot. Most of them have a single-axis measurement, and few are intended for monitoring normal and shear stress. This article proposes a low-cost, biocompatible triaxial piezoresistive sensor developed using simple fabrication techniques and inexpensive machinery. The sensor can detect pressures from 0-800kPa with high response and recovery with minimum hysteresis and repeatable results of over than 100 cycles.**

Keywords— 4D printing, tri-axial, tractile cell, flexible substrates, plantar shear force measurements

I. Introduction

The goal is to fabricate and test piezoresistive and capacitive sensors to measure plantar force in 3 planes. Such sensors need specific active and substrate materials, design, electrode configuration, encapsulation, and packaging to resist in-shoe environments and provide force-sensitive data in the x, y and z-axis. It is crucial to integrate the tri-axial tactile sensor to provide precise plantar measurements to sense the tri-axial contact forces between the feet and the ground. Asymmetries within the human body may induce gait imbalances. These imbalances are crucial to be monitored, therefore, adequate health care is provided promptly to avoid any adverse events to pre or post-operation patients with spinal cord injuries, hip and knee replacements, diabetic foot ulcers and so on [1],[2].

State-of-the-art tactile sensors are primarily made from inorganic silicon [3], [4], organic semiconductors [5][6][7], carbon nanotubes [8], graphene nanoplatelets [9], pressure-sensitive rubber [10], self-powered devices [11][12] are susceptible and can be applied to human skin. Yet, they require high-end workshops due to complex and expensive fabrication processes [13].

A variety of shear force-sensitive cells have been presented. Chase et al [14] developed a normal and shear force sensor with a one electrode at the top surface of the sensor and four electrodes at the bottom. The mechanical principle is formed by the deflection and compression forces of the filler layer between the top and bottom electrodes. The shear force and direction were computed using the fractions of the four capacitors. The disadvantage of this sensor is that it only measures a tiny delta in the capacitance, particularly when a shear force is applied.

Lei et al. [15] developed a capacitive pressure sensor for monitoring plantar force. The sensor consists of a top electrode, four bottom electrodes with a 'bump' layer, and a PDMS dielectric. Four independent capacitive sensing switches are formed, and values are averaged to enable measurements up to 945 kPa, even in non-uniform loads applied to the dielectric layer. Overall, these sensors have four capacitive elements, which can measure shear and normal forces through selective decoupling of the output signals. Using this approach, in 2013, Dobrzynska and Gijs [16] developed a flexible triaxial force sensor with "E"-shaped design for both the bottom and the top electrode. They consisted of four parallel-plate capacitors with a silicone dielectric. The cell can measure force in each axis up to 14 N (220 kPa), making it suitable for the range of pressure in plantar shear force measurements.

Wattanasarn et al. [17] developed a triaxial force sensor which is flexible and consists of four structures: a positive profile 'bump,' measuring coil, spacer and four excitation coils. When the sensor is not loaded, the same output voltage is present on the four measuring coils. The measuring coil is displaced on the application of load, resulting in differential voltage changes between the excitation coils. These can be selectively decoupled and used to calculate the applied force similarly to that used for triaxial capacitive sensors.

In general, these designs feature a certain challenge in measuring shear forces. Substrate integrity and electrode configuration must be arranged to detect shear forces independently. The substrate material implies to the material that contributes to the composite flexibility rather than the charge carrier [18]. The design principle focuses on the structural integrity of the substrate material, where it is reformed to detect normal and shear forces.

Lastly, Tao et al [19] developed a paper-based force sensor. Tissue paper was mixed with the graphene oxide (GO) solution to obtain a GO paper. Compared to the previously mentioned force sensors, it has obvious advantages in achieving ultrahigh sensitivity. The fabrication process is relatively easy and cheap to reproduce, and it was used to fabricate and test the initial proof of concept designs of the sensor illustrated in this paper. This led to the idea of using the art of folding and cutting paper, kirigami, to form the integrity of the substrate material. By folding paper, a slender material is formed which can easily bend but not easily stretched which leads to unique advantages such as structures designed around stretching are strong and lightweight [20]

The work was funded by Biederman Motech GmbH Co and partially supported by the Wellcome Trust [203145Z/16/Z].

This article has been accepted for publication in IEEE Journal on Flexible Electronics. This is the author's version which has not been fully edited and content may change prior to final publication. Citation information: DOI 10.1109/JFLEX.2023.3239052

The initial sensor concept design has been presented in the 2022 IEEE International Conference on Flexible and Printable Sensors and Systems (FLEPS) and was published in its Proceedings [21]. This article provides a detailed analysis of the mechanical and electrical model of the design and in addition, discusses the data visualisation software developed to interpolate the sensor data in an intuitive way to detect forces in 3-D and load distribution in a high-resolution 2-D heatmap.

II. Device Design and Materials

The design of the proposed device is illustrated in Fig. 1a. It consists of five different layers. The structure and materials shown as b, i, e_{top}, s, p, and e_{bot} indicate the thickness of the negative bump (silicone elastomer Mold Max™ 10), an insulation layer (Kapton tape), top electrode (copper tape), 3d printed semiconductive substrate (Ninjatek eel), PDMS (SYLGARD 184) spacer, and bottom copper electrode, respectively. The size of the cell is 10×10mm. One resistor is located on each corner of the substrate in each sensor cell to form a 2×2 array. The negative bump has four positive bumps at each corner of the cell and are aligned with the top electrode. The PDMS spacer is found in between the substrate and bottom electrode. The design of the substrate forms four gaps, as shown in Fig. 1c. The distance between the gaps, dt, on each corner is controlled by the direction of the applied force. The mechanism works like a biplanar seesaw where torque is generated at the four pivot points shown in Fig. 1c Two seesaw mechanisms are formed and respond to the shear force's direction when the moments on each four sides are uneven.

Subsequently, when the device is loaded at the top surface, the substrate is compressed, and the four air gaps between the electrodes decrease identically as shown in Fig 1e. This behavior suggests the four resistors have an equal resistance change. On the other hand, when the shear load is applied to one direction, the substrate produces a torque, incrementing the gaps for two resistors towards the applied shear force direction, as shown in Fig.1f, g. As a result, the applied normal and shear force can be sensed differently based on the resistance variation.

A 3D model of the device package was developed in Solidworks. To verify the mechanical principle the finite element method was used. The material properties were taken from datasheets from all materials forming the device [22],[23],[24]. The analysis was performed using an elastic model since the stress-strain curve of the materials used is almost linear, and the hysteresis is negligible for small deformations. Boundary conditions are applied at the bottom of the model with fixed supports in all directions. Contact surfaces were used between the pivot points referred to Fig. 1c and the opposed surface on the top. To simplify the analysis for computation cost with the trade of the compressibility effect, more contact surfaces sets were not used therefore the penetration shown cannot be avoided. The scope of the FEA is to show the mechanical principle of the sea-saw mechanism and not to find accurately the displacement induced. Figure 1e presents the application of normal (z) force across the whole top surface of the device illustrated from both side views. Shear pressures were applied in both x and y directions across the whole top surface of the device. As shown in Fig. 1f, g, the cell deforms as expected for shear pressures on the x and y-axis. Each side

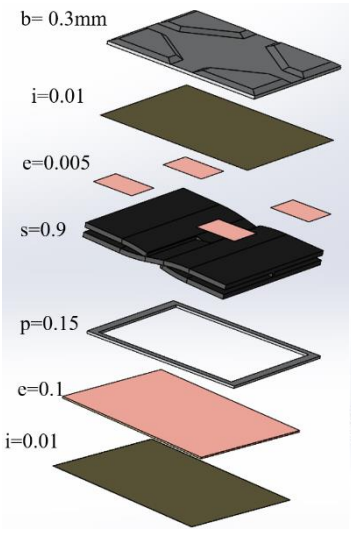

Fig. 1a Sensor layers

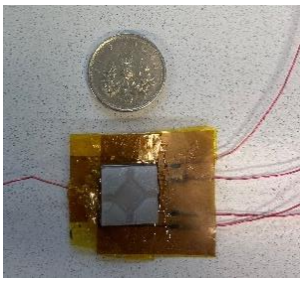
Fig. 1b sensor snapshot

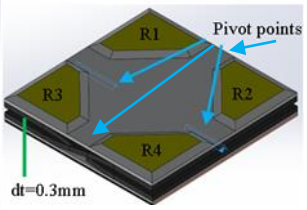

Fig. 1c Sensor composite structure annotating in yellow R1, R2, R3, R4 of each resistor, pivot points in blue and dt gap **distance** between the two substrates.

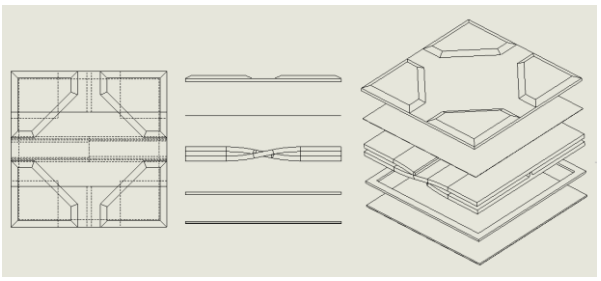
Fig. 1d Sensor design

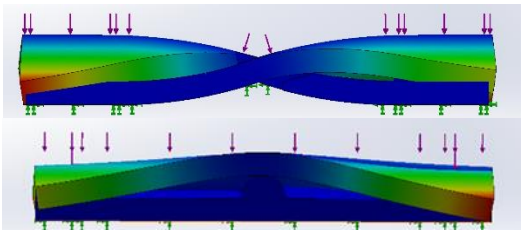
Fig. 1e Deformed part from normal force

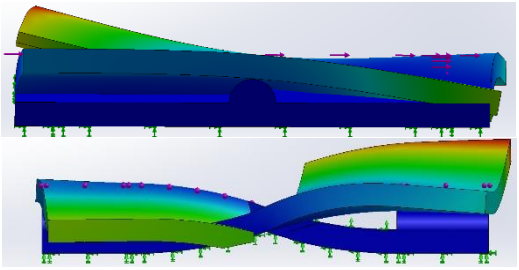
Fig. 1g Shear force on the x component

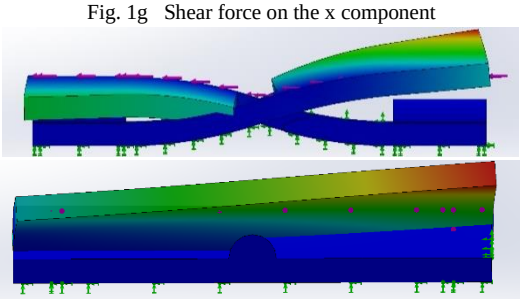
Fig. 1f Shear force on the y component

of the biplanar see-saw mechanisms responds to the direction of the shear force in a different manner.

III. PIEZORESISTIVE MODEL

The sensor was modelled using a simple approach of four resistors in parallel located at each corner of the sensor to translate the resistance change in the x, y and z axis. The four resistors in Eq. (1) are the four independent sensing elements located at the top side of the sensor for shear and normal loads detection.

$$\frac{\Delta R_1}{R_1}+\frac{\Delta R_2}{R_2}+\frac{\Delta R_3}{R_3}+\frac{\Delta R_4}{R_4}=\mathrm{Re} \quad (1)$$

The length of each wire connection in the circuit in Fig 2a was equal; therefore, it is assumed that wiring has no influence. Strain present on the x and y axis is negligible since the force applied to the device is compression, not tension. Therefore, on the z axis maximum strain is found. The areas of all four-square electrodes were designed identically with the area A = A1 = A2 = A3 = A4. The theoretical model assumes that the resistivity is equally thick across the entire sensor with a thickness of t when load is not applied and varies independently on each corner according to the load applied. Therefore, the resistivity Eq. (2) can be derived for the initial resistance Re as: where $\boldsymbol{\nu}$ and $\boldsymbol{\epsilon}$ are the Poisson's ratio and strain respectively and $\boldsymbol{\varrho}$ is the material's resistivity.

$$\mathrm{Re}=(1+2\nu)\varepsilon+\frac{\Delta\varrho}{\varrho} \quad (2)$$

A force in the z-direction reduces the distance by Δdt, decreasing all four resistors' resistance there Rz is the sum of all resistors as in Eq. (3). A force in the x-direction increases the thickness of the resistor R1 by Δdt and decreases the thickness of R3 to the same extent while not influencing R2 and R4. A subtraction of each pair of resistance indicates the applied shear forces in the x- and y-direction, as shown in Eq. (4)(5).

$$Rz=R1+R2+R3+R4=\frac{dt_{R1}+dt_{R2}+dt_{R3}+dt_{R4}}{t} \quad (3)$$

$$Rx=R1-R3=\frac{dt_{R1}-dt_{R3}}{t} \quad (4)$$

$$Ry=R2-R4=\frac{dt_{R2}-dt_{R4}}{t} \quad (5)$$

A piezoresistive analysis was performed in ANSYS to investigate the effect of displacement induced from load within the substrate versus the electric potential. For simplicity, 2-d analysis was performed by modelling the substrate as a rectangular shape with dimensions of 0.9mm thick and 10mm long. The element type used was coupled-field 10-node tetrahedron. Positive and negative terminals were set at the rectangle's top and bottom, respectively. The model was fixed from the bottom and loaded from the top with 800kPa. The elasticity and resistivity of the substrate are isotropic; therefore, a volume resistivity of 15000 ohms was used. Data for displacement and electric potential was taken from nodes across the vertical side on the right-hand side. The deformed shape behaves elastically up to 12Mpa pressure as shown in Fig 2b, c. The results in Fig.2d, e illustrate that electric potential within the substrate media is directly proportional to the load applied to the sensor.

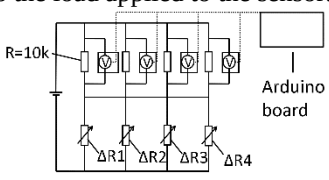

Fig. 2a Circuit schematic

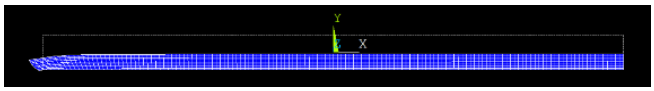

Fig. 2b Deformed and undeformed shape

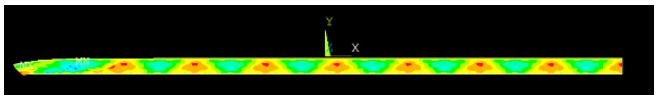

Fig 2c Deformed shape vs electric potential

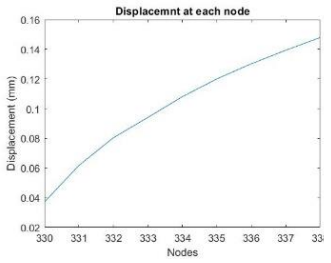

Fig. 2d Displacement plot at each node

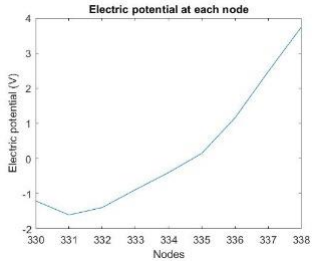

Fig. 2e Electric Potential plot at each node

IV. SURFACE TREATMENTS AND PACKAGING

The device comprises of two identical semiconductive substrates in a sandwich-like design as shown in Fig. 3. The design was done in Solidworks and the material used was TPU Eel carbon nanotubes fused filament. Ninjatek Eel is a flexible conductive filament, consists of thermoplastic polyurethane (TPU) doped with carbon-black, produced by Ninjatek with a hardness of 90 A, tensile strength of 12 Mpa, elongation at the strength of 355%, and surface electrical resistance of $1.5 \cdot 10^3$, by ANSI/ESD STM 11.1.

Wet etching was performed to shape the electrodes using copper and Kapton tape. Firstly, the two tapes were adhered together, avoiding any air bubbles in between, as shown in Fig. 3a. A photosensitive film was applied on copper surface and a mask of the positive profile of the desired electrode location with its connection traces and pads. Then, photolithography penetrated the film, leaving the electrode configuration's negative profile Fig. 3b, c. A positive developer (NaOH) was used to remove the mask's penetrated traces Fig. 3d. The etching process follows where the PI-Cu laminate was exposed to Ferric chloride acid Fig.3e. This results in a 5.5 µm thick copper electrode with 6.3µm of insulation. Finally, wires are soldered to the copper pads in the PI-Cu laminate. PDMS spacer was molded by mixing the two parts and degassing them. The uncured silicone was poured on a flat surface and agitated using an orbital shaker to form a thin layer for the spacer. Then, it was placed in a convection oven at 80 $°C$ for approximately 1 hour 30 minutes until the PDMS was completely dry. When cured the PDMS is cut using square-shaped hole punchers. Silicone MoldMax 10T was used as an encapsulated layer at the top,

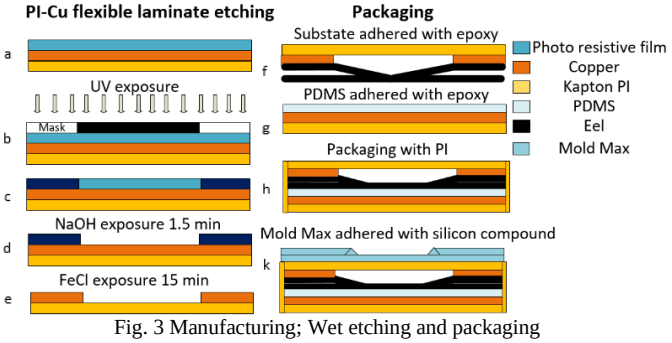

Fig. 3 Manufacturing; Wet etching and packaging

and by the molding method the desired design was achieved. Packaging was done manually by stacking part g and f with the encapsulation on top, as shown in Figure 3f-k.

V. Data Visualisations

A Python code has been developed for the visualise of real-time data of the pressure sensor. The code consists of importing the data from an Arduino board and using them to create a 3D schematic representation of the forces that act when pressure is applied. Specifically, the Arduino ports were connected, and numerical/mathematical libraries were imported to aid the analysis. The Rx, Ry and Rz components of the applied force were imported from an Arduino board, and the values were appended into three lists (one for each dimension). An algorithm has been written for calibration needs that takes the initial x, y and z values without applying any pressure on the sensor and converts them to zero so that the force applied is shown as none, which is the actual case. These initial values were then subtracted from every reading to use the real applied force.

Once the calibration was done, a white scene with a black box representing the sensor as created as shown in Fig. 4b. An arrow was also produced that points to the direction of the applied force in 3-D. Moreover, the size of the arrow scales like the value of the force applied i.e., for a small, applied force, the arrow appears small, and for a bigger applied force, it appears to be larger. Additionally, using spherical polar coordinates as shown in Fig.4a, the total force magnitude, as well as the theta (θ, angle between the force vector and the normal to the sensor) and phi (φ ,angle measured clockwise between the force vector and the North) angles have been calculated using cartesian coordinates, as shown in Eq. 5, 6, 7 [25].

$$r = \sqrt{x^2 + y^2 + z^2} \tag{5}$$

$$\theta = arccos\frac{z}{\sqrt{x^2+y^2+z^2}} = arcos\frac{z}{r} = arctan\frac{\sqrt{x^2+y^2}}{z} \tag{6}$$

$$\varphi = \begin{cases} arctan\frac{y}{x} & if\ x \geq 0 \\ arctan\frac{y}{x} + \pi & if\ x < 0 \end{cases} \tag{7}$$

Other than the force projection simulation explained above, the sensor signals can also be used to visualise normal forces in a high-resolution image. The sensor can detect only normal forces when interpolating the results using heatmap visualisation. Commercial force-sensitive sensors have a single output, which means single pixel data. Multiple commercial sensors need to be used to form an image of pressure distribution. The proposed sensor can only form up to 64 by 64 pixel image using four analogue channels from one sensor. The explanation to interpolate the results as shown in Fig. 11, is as follows: (1) Three arrays have been created: one for each axis (x, y & z). Each array consists of 50 random points between -30 and 30, representing the coordinate position. (2) A 2D mesh grid has been created between the maximum and minimum x-y values (i.e. -30 and 30 in this case), using 1000 points. (3) For each coordinate value, (xi, yi, zi), a Gaussian has been produced which scales as the force in the z/downwards direction i.e. zi component. This means the Gaussian will appear higher for a larger force, and shorter for a smaller force. (4) The following Gaussian equation has been used, where x is the x-component of the force, y the y-component, z the z-component and w the width of the Gaussian:

$$Gaussian(x, y, z) = e^{-\frac{x^2+y^2}{w^2}} \tag{8}$$

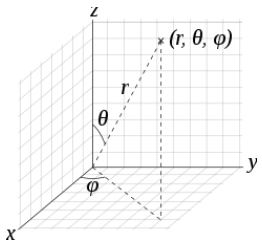

Fig. 4a Cartesian coordinates

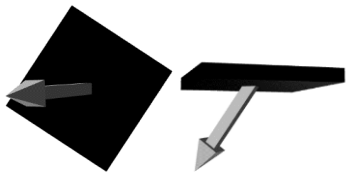

Fig. 4b Force projection arrow

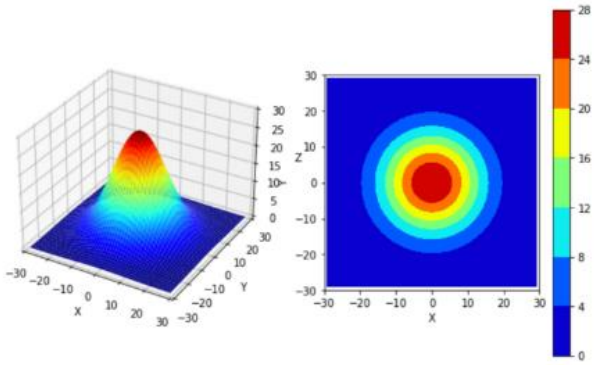

Fig. 4c 2-D heatmap visualisation

(5) The width (w) of the Gaussian has been set to change according to the force in the x,y component, as in the case of the Gaussian's height. (6) For each (xi, yi, zi), a new figure has been created so that the simulation updates as the loops iterate. (7) The heatmap's colour bar also represents the strength of the downwards force. Red corresponds to a large force, green corresponds to a gentle force, and blue corresponds to a weak force. (8) The resulting 3D plot shows a fixed x-y mesh grid, where the Gaussian updates according to the x, y & z forces imported from the sensor.

VI. Experimental Results and Discussion

A. Device perfrormance characteristics

Device performance characteristics were tested using a universal Mechanical test machine (Zwick Roel). The whole surface of the cell was covered with a rigid indentor and a known force was applied. The cell was supported at the bottom to a silicone slab to simulate the mechanics of plantar forces as the application of the human foot is striking the shoe elastomer and not the ground. Power supply was used at 5V, 0,3A DC connected to the bottom electrode of the device and TEKTRONIX 4 channel oscilloscope was used to measure the voltage change on the top electrodes through a voltage divider circuit. Firstly, to find hysteresis, response, recovery, repeatability, and fatigue resistance of voltage change, a cyclic fatigue test was performed. A constant load of 10N with 300ms hold was applied for 100 cycles. Secondly, a creep test was prompted to find the voltage relaxation by holding a constant load of 20N for 1 hour. Thirdly, the sensitivity of the tactile cell was found using a stepwise load test ranging from 1 to 80N, with increments of 1N per step. Lastly, by supplying a constant current for 1 hour, zero drift time was found.

Table 1 summarises the overall performance of the sensor cell. Figure 5a illustrates the sensitivity of the sensor from the stepwise load test. The sensor appears linear in two regions, one between 0-200kPa with ~100 Pa/mV and another from 200 to 800kPa with 375 Pa/mV. Consequently, the cell is almost four times more sensitive to low pressures

This article has been accepted for publication in IEEE Journal on Flexible Electronics. This is the author's version which has not been fully edited and content may change prior to final publication. Citation information: DOI 10.1109/JFLEX.2023.3239052

Table 1 Sensor characteristics

Performance	Specifications
Hysteresis	2%
Response	100ms
Recovery	150ms
Repeatability	4%
Fatigue resistance	100 cycles
Relaxation	5% / 30min
Zero drift time	0.5% / h

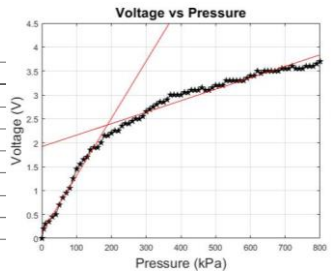

Fig. 5a Sensor sensitivity

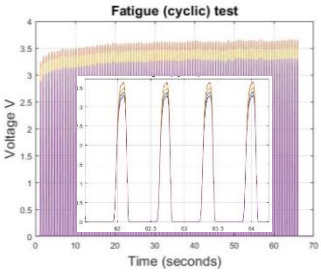

Fig. 5b Cyclic test raw data

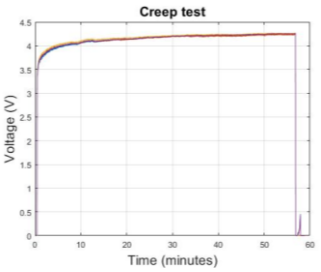

Fig. 5c Creep test raw data

Than to higher pressures. Nevertheless, by tuning the calibration algorithm in the simulation explained, the force range sensitivity makes the sensor suitable for plantar measurement. Although, peak pressures of heavy-weightusers could be a problem. The force range could be customised upon the task by altering the percentage infill of 3d printing or the thickness of the substrate materials, which will be explained later. Figures 5b and c show the raw data from the cyclic fatigue test and creep load. It is observed the bespoke parameters satisfy the needs of plantar measurements. Specifically, the fatigue test showed that for calibration, a "warm-up" of ten cycles must be loaded when the sensor is first connected to obtain repeatable results. It has been observed that after ten cycles, repeatability is within 4%. The deviation percentage of the signal form the 11th cycle to the last was used to derive the repeatability of the sensor. It is important for the sensor to supply repeatable results for a constant load. The creep test illustrates that sensor relaxation has 5% deviation in 30 minutes of continuous constant load. The PDMS spacer improves hysteresis, allowing the sensor to restore the open circuit when no load is applied. The zero drift time was tested by capturing data from the sensor continuously for one hour without any load application. This was performed to test the deviation percentage of the signal when current passes through the device for long periods of time.

Another experimental set-up was used to apply shear force in four directions to calibrate the relation between voltage and force applied in the planar plane (shear). The set-up consists of 3 axes linear controlled test rig with a 3-d printed indentor. Deflection of the indentor is measured using commercial implant strain gauges, which are highly sensitive and accurate. They were glued 60mm away from the point of load application to measure the strain change while the indentor was applying shear force on the sensor cell. The motion of the end effector is controlled automatically, moving in each axis from one corner to the other, as shown in Fig. 6a, b, from 0mm to 10mm. Therefore, the total deflection of the beam on the y axis is 10mm. Data collected from strain gauges and sensor cells were synchronised and analysed for comparison. A strain gauges were used to measure the strain within the

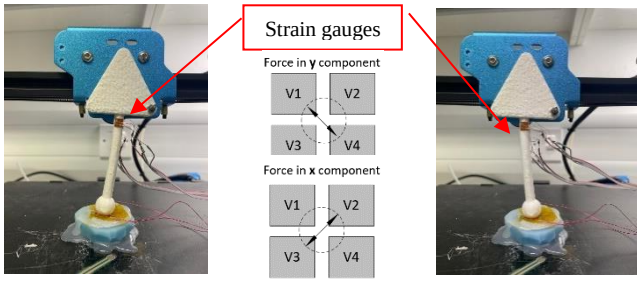

Fig. 6 a, b Indentor load motion

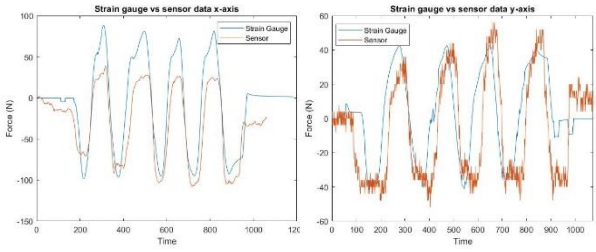

Fig. 6 c, d Synchronised strain and sensor force data on the x-axis and y axis

indentor along each direction and the applied shear force can be found using the formula simple elastic bending beams where y is the deflection, M moment induced, E the Young's Modulus and I the inertia.

$$\frac{strain}{M} = \frac{y}{EI} \tag{9}$$

Initially, the force was applied on the top surface of the cell acting on the z-axis, followed by shear force on the x and y-axis, as shown in Fig 6xa, b. Fig 6c depicts the force calculated using eq.9 from the data recorded from the strain gauge versus sensor data for the x-axis. The x-axis shear load results show that voltage changes in sensing elements V1~V3 are much more significant than V2~V4. Also, V1 and V3 are out of phase; by taking the difference between them, shear load data can be obtained. Data shown in Fig. 6c, d is synchronised with the strain gauge data and behaves almost identical. Similarly, the y-axis shear load results in Fig. 6d show the same behaviour when a shear load is applied. By taking the difference of values in V2~V4, the shear load can be obtained from the sensor.

B. Data Visualization Validation Tests

To validate the accuracy of the force projection arrow from the simulation explained earlier, a rigid 2 DOF test rig was assembled carefully. To apply force at an angle, the test rig contains a hinge joint and a linear actuator as shown in Fig. 7a. The actuator is controlled with an Arduino, a driver board, and forward, reverse, stop switches. The sensor cell is attached to a rotating platform measured with an analogue goniometer. The same tool was used to measure the angle of the hinge joint. Constand load is achieved at various angles, which made it suitable to validate the accuracy of the force projection found from the simulation. Constant load was applied at 10,20,30,40° for θ angle and 90,180,270,360 for φ angle. Data was collected using an Arduino which enables connection to the simulation in Python. Text files of force,

This article has been accepted for publication in IEEE Journal on Flexible Electronics. This is the author's version which has not been fully edited and content may change prior to final publication. Citation information: DOI 10.1109/JFLEX.2023.3239052

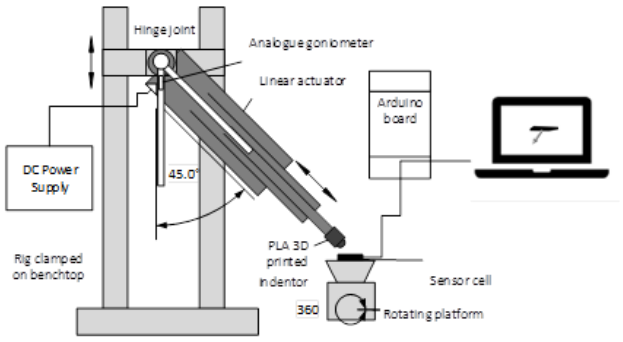

Fig. 7a Test rig to validate computed force angle projection

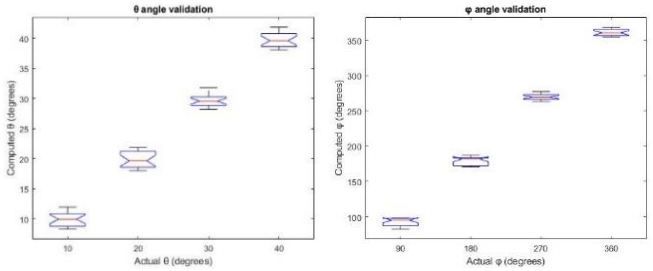

Fig. 7b, c ANOVA results for θ and φ angle

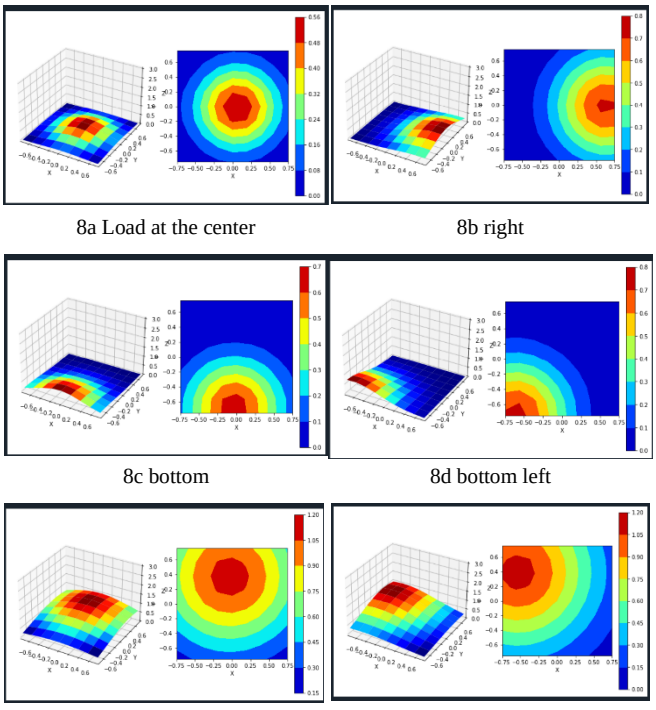

8a Load at the center 8b right

8c bottom 8d bottom left

8e top 8f top left

Fig. 8a, b, c, d, e, f Heat map results on each location test.

angle θ and φ were exported and 20 data points from each dataset were used to perform a one-way ANOVA test. By plotting the variance, the accuracy of the measurements is within a sensible range to deduct accurate reading for inverse kinetic calculations as shown in Fig7c, d. It was observed that the sensitive range of θ and φ are within ±45º and ±180º, respectively.

The accuracy of the heatmap simulation was validated by applying constant pressure using a 4mm diameter spherical indentor at various sensor locations starting from the center. The location of the load application is identical to the heat map result as shown in Fig 8a, b, c, d, e, f.

C. Scalability experiments

Further experiments were conducted to explore printing modifications' efficacy for other applications requiring different pressure ranges. The conductivity of the 3d printed substrate media can be modified to the desired pressure range sensitivity. There are two methods this can be done, first by changing substrate thickness and second by adjusting the percentage printing infill of the 3d printer.

By increasing the thickness of the substrate, the distance between active layers is increased, and due to the elastic properties of the substrate, higher compression forces are susceptible to the structure. Therefore, thicker substrates are sensitive to higher pressures and thinner substrates to lower pressures. Below the graphs show a stepwise load test from 0-120N with increments of 4N each step. Thicker substrates are less conducive since there is a more significant gap between active layers (copper), allowing a higher-pressure measuring range. The saturation point is at 5V where saturation is the point when maximum strain is induced from high forces within the structure, causing resistance to decrease to the minimum. The sensor behaves as a closed-circuit hence 5Vin=5Vout. At 120N, the 0.3mm sensor reads a value at 2.5V and the 0.7mm at 1V as observed in Fig 9a. Until saturation point, the 0.7mm sensor will detect much higher pressures.

In addition, a high percentage of printing infill enables higher conductivity within the substrate, thus sensitive to lower forces, and alternatively, low infill is sensitive to lower forces. Figure 9b shows two sensors with different printing infill injected with 12V 0.3A. It can be observed that lower infill has a decreased sensitivity to lower forces and can be sensitive to higher forces since the point of saturation is at 12V. In contrast, the 100% infill saturates at 12V when 120N is applied to the sensor. Images of 100% and 80% printing infill taken from a Keyence VH-Z100R are shown in Fig. 9c and d, respectively.

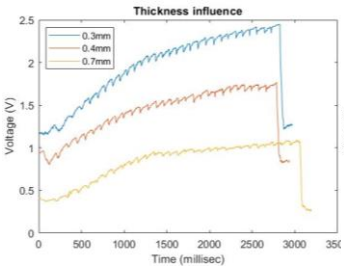

Fig. 9a Sensitivity change of different thicknesses of 3-d printed substrate

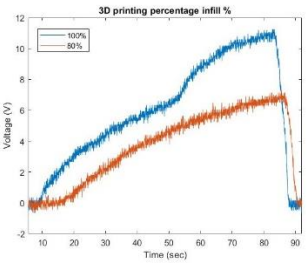

Fig. 9b Sensitivity change of different percentage infill of 3-d printed substrate

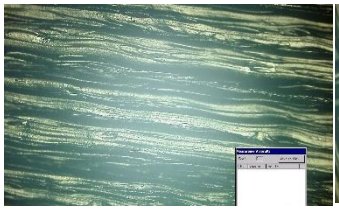

Fig. 9c 100% printing infill

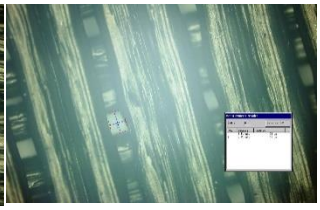

Fig. 9d 80% printing infill

VII. Conclusion

This article has described the design and development of a low-profile planar sensor that can measure shear and normal load (pressure). The goal is to develop an instrumented shoe insole with an array of the sensors to measure ground reaction force and the foot's centre of pressure. The desired sensor performance for such an application is withing a pressure range of 0-740kPa for normal forces, 0-140kPa for shear forces and sampling rate of 50Hz during normal walking. As presented in this paper the sensor proposed is able to support the desired performance. While designed primarily for in-shoe application, the device could be used for measuring shear forces between any adjacent surfaces where a small, low-profile sensor is needed. This new sensor has many potential applications; in the healthcare sector, it could be integrated in wearables, prosthetics, surgical robot haptics, and artificial pressure-sensitive skins such as data gloves. It could be used more widely in any industrial applications such as in load cells of triaxial mechanical test machines or industrial assembly line robots for fine grasp control. A third sector which could benefit is sport industry, for example, collecting data from athletes to analyse their training performance especially in running and football. As mentioned in this paper, alterations could be made to fit the requirements of each of these different applications. Overall, the device shows promising results with reliability although part to part reproducibility can be improved by using dual extrusion printing. Printing insulating and semiconductive materials at the same time you can achieve reproducible and complex designs. This method creates self-packaged devices which will be used in future developments.

Acknowledgment

The authors are grateful to our sponsors and towards the Institute of Orthopaedic and Musculoskeletal Science technical team at UCL for their support and to Prof Steve Taylor for his help and assistance. This work is supported by the Wellcome/EPSRC Centre for Interventional and Surgical Sciences (WEISS) (203145/Z/16/Z).

References

[1] Wang, L. et al (2020). A Review of Wearable Sensor Systems to Monitor Plantar Loading in the Assessment of Diabetic Foot Ulcers. IEEE Transactions on Biomedical Engineering, 67(7).

[2] Yavuz, M., Master, H., Garrett, A., Lavery, L. A., & Adams, L. S. (2015). Peak plantar shear and pressure and foot ulcer locations: A call to revisit ulceration pathomechanics. In Diabetes Care (Vol. 38, Issue 11).

[3] Kim, D. H., Lu, N., Huang, Y., & Rogers, J. A., "Materials for stretchable electronics in bioinspired and biointegrated devices." MRS Bulletin, 37(3), 2012.

[4] Takei, K., Takahashi, T., Ho, J. C., Ko, H., Gillies, A. G., Leu, P. W., Fearing, R. S., & Javey, A., "Nanowire active-matrix circuitry for low-voltage macroscale artificial skin." Nature Materials, 9(10), 2010.

[5] Kaltenbrunner, M., Sekitani, T., Reeder, J., Yokota, T., Kuribara, K., Tokuhara, T., Drack, M., Schwödiauer, R., Graz, I., Bauer-Gogonea, S., Bauer, S., & Someya, T., "An ultra-lightweight design for imperceptible plastic electronics". Nature, 499(7459), 2013.

[6] Chortos, A., Lim, J., To, J. W. F., Vosgueritchian, M., Dusseault, T. J., Kim, T. H., Hwang, S., & Bao, Z., "Highly stretchable transistors using a microcracked organic semiconductor." Advanced Materials, 26(25), 2014.

[7] Someya, T., Sekitani, T., Iba, S., Kato, Y., Kawaguchi, H., & Sakurai, T., "A large-area, flexible pressure sensor matrix with organic field-effect transistors for artificial skin applications." Proceedings of the National Academy of Sciences of the United States of America, 101(27), 2004.

[8] Yamada, T., Hayamizu, Y., Yamamoto, Y., Yomogida, Y., Izadi-Najafabadi, A., Futaba, D. N., & Hata, K., "A stretchable carbon nanotube strain sensor for human-motion detection." Nature Nanotechnology, 6(5), 2011.

[9] Li, X., Zhang, R., Yu, W., Wang, K., Wei, J., Wu, D., Cao, A., Li, Z., Cheng, Y., Zheng, Q., Ruoff, R. S., & Zhu, H., "Stretchable and highly sensitive graphene-on-polymer strain sensors." Scientific Reports, 2, 2012.

[10] Mannsfeld, S. C. B., Tee, B. C. K., Stoltenberg, R. M., Chen, C. V. H. H., Barman, S., Muir, B. V. O., Sokolov, A. N., Reese, C., & Bao, Z., "Highly sensitive flexible pressure sensors with microstructured rubber dielectric layers." Nature Materials, 9(10), 2010.

[11] Wu, W., Wen, X., & Wang, Z. L., "Taxel-addressable matrix of vertical-nanowire piezotronic transistors for active and adaptive tactile imaging." Science, 340(6135), 2013.

[12] Wang, Z. L., "Self-powered nanosensors and nanosystems." Advanced Materials, 24(2), 2012.

[13] T. A. T. A. Chase and R. C. R. C. Luo, "A thin-film flexible capacitive tactile normal/shear force array sensor," in Proceedings of IECON '95-21st Annual Conference on IEEE Industrial Electronics, pp. 1196–1201, Orlando, FL, USA, 1995.

[14] Yang, T., Xie, D., Li, Z., & Zhu, H. (2017). Recent advances in wearable tactile sensors: Materials, sensing mechanisms, and device performance. In Materials Science and Engineering R: Reports (Vol. 115).

[15] Lei, K. F., Lee, K. F., & Lee, M. Y., "Development of a flexible PDMS capacitive pressure sensor for plantar pressure measurement. Microelectronic Engineering, 99, 2012.

[16] Dobrzynska, J. A., & Gijs, M. A. M., "Polymer-based flexible capacitive sensor for three-axial force measurements." Journal of Micromechanics and Microengineering, 23, 2013.

[17] Wattanasarn, S., Noda, K., Matsumoto, K., & Shimoyama, I. (2012). 3D flexible tactile sensor using electromagnetic induction coils. Proceedings of the IEEE International Conference on Micro Electro Mechanical Systems (MEMS).

[18] H. Yao, J. Ge, C. Wang, X. Wang, W. Hu, and Z. Zheng, "A Flexible and Highly Pressure-Sensitive Graphene – Polyurethane Sponge Based on Fractured Microstructure Design," pp.6692–6698, 2013.

[19] Tao, L. Q., Zhang, K. N., Tian, H., Liu, Y., Wang, D. Y., Chen, Y. Q., Yang, Y., & Ren, T. L. (2017). Graphene-Paper Pressure Sensor for Detecting Human Motions. ACS Nano, 11(9).

[20] Elder, T., Rozairo, D., & Croll, A. B. (2019). Origami Inspired Mechanics: Measuring Modulus and Force Recovery with Bent Polymer Films. Macromolecules, 52(2).

[21] C. Heracleous, J. J. Leong and R. C. Loureiro, "Scalable 4-D printed tactile sensor for the detection of shear forces in the aid of plantar measurements," 2022 IEEE International Conference on Flexible and Printable Sensors and Systems (FLEPS), 2022, pp. 1-4

[22] SYLGARD™ 184 Silicone Elastomer "Technical data sheet: https://www.dow.com/content/dam/dcc/documents/en-us/productdatasheet/11/11-31/11-3184-sylgard-184-elastomer.pdf?iframe=true"

[23] Silicone elastomer Mold Max™ 10 "Technical data sheet: https://www.smooth-on.com/msds/files/823A-231B.pdf

[24] Ninjatek eel 3d printer filament "Technical data sheet: https://ninjatek.com/wp-content/uploads/Eel-TDS.pdf"

[25] https://en.wikipedia.org/wiki/Spherical_coordinate_system